

Morphological Image Processing and Network Analysis of Cornea Endothelial Cell Images

Luc Vincent

Xerox Imaging Systems

9 Centennial Drive, Peabody, MA 01960

Barry Masters

Department of Anatomy and Cell Biology

Uniformed Services University of the Health Sciences, Bethesda, MD 20814-4799

Abstract

In this paper, we propose a robust and accurate method for segmenting grayscale images of corneal endothelial tissue. Its first step consists in the extraction of markers of the corneal cells using a dome extractor based on morphological grayscale reconstruction. Then, marker-driven watershed segmentation yields binary images of the corneal cell network. From these images, we derive histograms of the cell sizes and number of neighbors, which provide quantitative information about the condition of the cornea. We also construct the neighborhood graph of the corneal cells, whose granulometric analysis yields information on the distribution of cells with large number of neighbors in the tissue. Lastly, these results help us propose a model for the corneal cell death phenomenon. The numerical simulation of this model exhibits a very good match with our experimental results. This model not only allows us to refine our understanding of the phenomenon: combined with our results, it enables the estimation of the percentage of cells having died in a given corneal endothelial tissue.

1 Introduction

The human cornea is a 500 microns thick, transparent tissue which covers the anterior surface of the eye. The cornea and the ocular lens are the refracting elements of the eye. At the posterior side of the cornea is situated a single, connected layer of endothelial cells. These cells, polygonal in shape, are about 20 microns across and about four microns thick. At birth, the corneal endothelial cells are all hexagons. Cells die as the cornea ages, but there is no new cell division when a cell die: instead, the surrounding cells elongate to fill in the gap and therefore, the average size of the endothelial cells increases throughout life. The corneal endothelial cells are responsible for the maintenance of corneal transparency; active transport enzyme systems pump ions into the regions between the cells, the resulting osmotic force drives fluid out of the cornea into the aqueous humour. In the normal eye, the fluid transport is in balance with the fluid transport leakage from the aqueous humour into the cornea and corneal transparency is maintained. In diseased or injured corneas, this balance is disturbed and the cornea swells and loses its transparency. The analysis of corneal endothelial cell size and shape is extremely important for diagnostic purposes.

In this paper, we propose a new and robust method to segment grayscale images of corneal endothelial cell tissue. This method is based on advanced morphological transformations [18, 19], including grayscale reconstruction [25] and watersheds [2, 27]. It allows us to precisely and robustly extract the cell outlines, which is the first step towards the automatic analysis of corneal tissues. This method is described in the section 4.

In section 5, we first derive shape and size measurements from the obtained binary images. Histograms of cell sizes and number of edges turn out to convey a lot of information on the corneal condition. We then build neighborhood graphs on the corneal tissue and use morphological granulometries of these graphs [13, 21] to study the distribution of large and small cells within the tissue.

Lastly, in section 6, we model the cell death phenomenon. Numerical simulations of this model exhibit a very good match with the results found experimentally in section 5. Comparing the measurements on a given corneal tissue with the model allows us to estimate the percentage of cells having died, and therefore provide a good estimate of the condition of the cornea.

2 Previous work

Several previous studies have reported attempts to use computer assisted image analysis in order to extract cell size and shape from photomicrographs of the human cornea endothelium. The main problem has been the location of the cell boundaries in the gray level image obtained from a photograph or a digitized video frame.

The initial work on the problem of edge detection is represented by the works of Laing et al. [10] and Fabian et al. [4]: photographs or video images were digitized and histogram manipulation followed by thresholding was used for edge detection of the cell boundaries. More elegant image processing techniques were recently proposed by Cazuguel et al. [3]: histogram equalization, top-hat filter followed by skeleton by influence zones [11], and Yu et al.: adaptive local enhancement, low pass filter and matched filters with kernels corresponding to different orientations...

Still, none of these solutions seem to be robust enough to deal with a vast variety of initial images (contrast, noise level, lighting conditions may greatly vary from one case to the other). Furthermore, there remains a lot of work to be done on the interpretation of the results (i.e., of the binary images obtained after segmentation). To our knowledge, no published work has ever gone beyond the simple measurement of cell areas and number of neighbors.

3 Data Acquisition

In our study, a corneal wide-field specular microscope [9, 17, 14] was used to obtain the gray level images of a field of several hundred cells from normal human patients. The principle of the microscope is that a slit of light is imaged on the cornea and the region of the interface between the endothelial cell layer and the aqueous humour exhibits a high reflectivity due to the shape change in refractive index. The microscope operated in the specular mode: the specular reflection of light from the boundary between the endothelial cells and the aqueous humour forms the image. The cell borders have stronger specular reflection than the other regions of the cells and this generates the image contrast. The scattered light from this interface is imaged onto a film plane in a camera. A flash of light is used to eliminate motion effects on the image. The design of the specular microscope eliminated the bright surface reflection from the air-cornea surface, since an applanating microscope objective is used to match the refractive index to the cornea. An example of the images of our test suite is shown in Fig. 1.

4 Segmentation

We illustrate our segmentation technique on a smaller image, shown in Fig. 2(a). Notice the very irregular lighting, which makes it impossible to use any direct thresholding mechanism. On this image and in Fig. 1, one can also observe that the cells can vary quite a bit in size. This remark becomes even more true with damaged or diseased cornea. Nevertheless, the cells form a contiguous partition of the space: the separation between any two neighboring cell is a thin dark line of relatively constant thickness. Therefore, it seems natural to try to detect these dark cell outlines using the top-hat transformation.

The top-hat transformation is a morphological segmentation tool which was originally described in [15]. In its valley-detection version, it consists of subtracting the image I under study from I closed by a given structuring

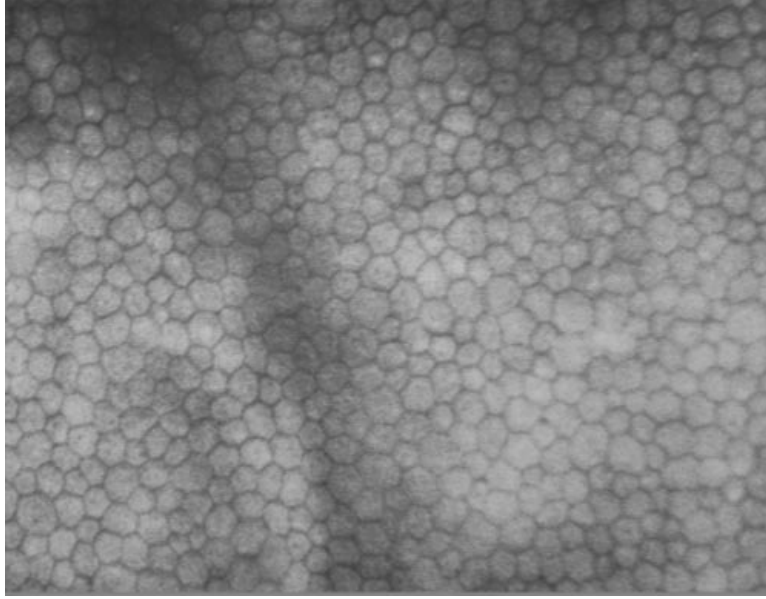


Figure 1 : *Image of a corneal endothelial cell tissue.*

element [18]. Here, a top-hat of Fig. 2(a) with respect to a small disc yields Fig. 2(b), where the cell separations appear clearly.

However, due to the variations in contrast from the center of the image to, e.g., the top right corner, it is impossible to set a correct threshold for this image: the threshold shown in Fig. 2(c) is appropriate for the center of the image, but on the top corners, the network of cell boundaries gets disconnected. On the other hand, a lower threshold value would correctly extract the cell outlines in the top part of the image, but overconnect the network in the central area. Furthermore, in each of the images we looked at, the “best” threshold value highly depended on the image contrast and always had to be manually adjusted. Therefore, although it is at the basis of already published work [3], we did not retain the top-hat transformation in our final segmentation algorithm.

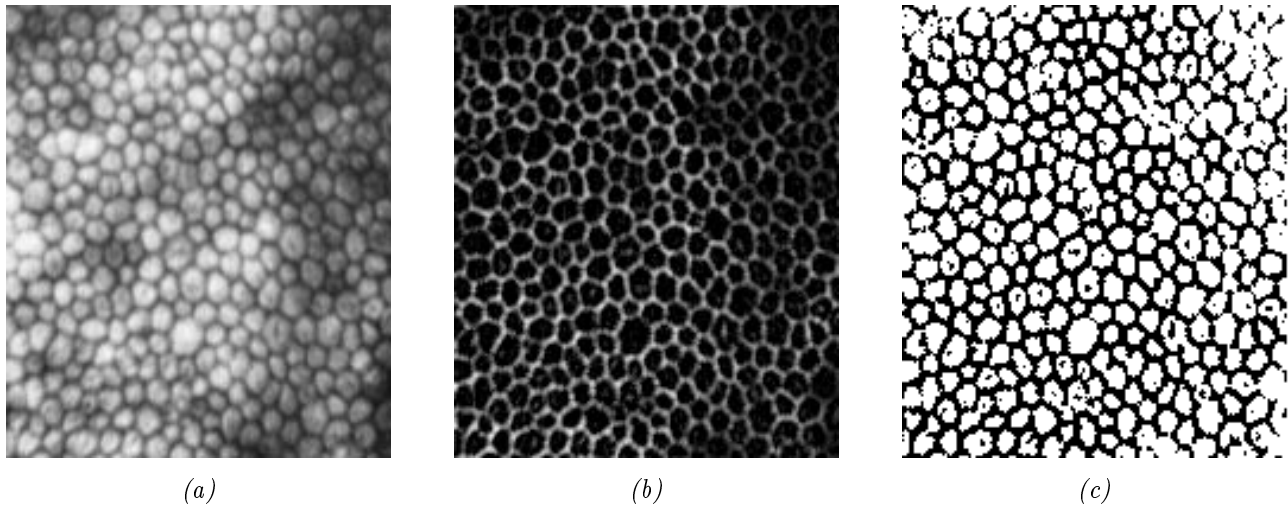


Figure 2 : *Image used to illustrate our segmentation method (a), top-hat (b) and threshold of this top-hat (c).*

Instead, we chose to first preprocess our images using a simple morphological filter in order to remove the impulse noise while preserving the valleys (separating lines between cells). An alternated sequential filter (ASF) of small size

[19, 20] was chosen for this purpose. Following this operation, we were able to verify that:

|| The difference between the maximal gray-level on one cell and the maximal gray-level in the surrounding valley is always greater than a threshold h .

In our test images, the threshold h was always greater than 10 gray levels.

Following this remark, to detect the cells, we do not take any size information into account but solely rely on contrast. The principle is to subtract constant h from original image I , and to compute the *grayscale reconstruction* of I from $I - h$. Morphological reconstruction is part of a set of operators referred to as *geodesic transformations* [12]. Let us denote $\delta(J)$ the unit dilation of a grayscale image J (i.e., the dilation by the elementary ball of the considered grid) and $\delta_I(J)$ the elementary geodesic dilation of I under J , i.e.:

$$\delta_I(J) = \delta(J) \wedge I.$$

(\wedge being the pointwise minimum). The following definition of grayscale reconstruction can be proposed [25]:

Definition The grayscale reconstruction $\rho_I(J)$ of I from J is obtained by iterating grayscale geodesic dilations of J “under” I until stability is reached, i.e.:

$$\rho_I(J) = \lim_{n \rightarrow +\infty} \underbrace{\delta_I \circ \delta_I \circ \dots \circ \delta_I}_{n \text{ times}}(J).$$

$\rho_I(I - h)$ is shown in Fig. 3(a). The result of subtracting $\rho_I(I - h)$ from I is the image of the so-called h -domes of I (see Fig. 3(b)). A threshold, chosen to be a fixed percentage of the original constant h (33% here), is then applied, yielding Fig. 3(c). This image is called marker-image: every cell of the original image is represented in it by a unique connected component. The dome extraction method used for this marker extraction step was originally developed by M. Grimaud and is described in a broader framework in [6]. Examples of its use are also described in [22, 27, 5].

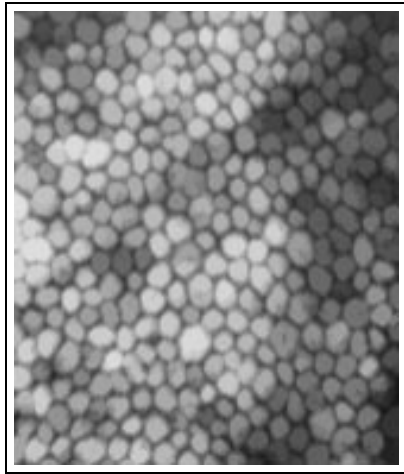
Having extracted good markers of our objects, the cells, we can now perform *watershed* segmentation. The watershed transformation is a very powerful morphological operation which was introduced in [2], and whose use for segmentation was described and illustrated in numerous recent publications [16, 26, 27]. Given a set of markers and an image f regarded as a topographic relief, a “marker-driven” watershed segmentation allows the image analyst to extract the highest crest-lines of f separating two markers. Usually, one chooses for f a gradient-image, since the object’s contours can be seen as the highest crest-lines of the gradient around the object’s marker. However, in our particular case, the cells form a contiguous tessellation of the space, and we want to extract the network of their separating lines. These lines are the deepest valley lines separating our markers and are thus extracted by using as image f the opposite of original image 2(a) (see Fig. 3(d)). The result of this watershed segmentation is shown in Fig. 3(e) and in Fig. 3(f), superimposed to the original corneal tissue.

Except for a few cases (namely 5 in our example) where cells have been broken in two, the segmentation is perfect: the use of the watersheds assures that the extracted valley lines are optimal with respect to the set of markers controlling the segmentation. In particular, observe that the segmentation is not only correct in the central area, but also in the top-right corner. Importantly, no elaborate preprocessing was required for this segmentation: by improving this aspect of the process, we extract better markers, which immediately results in better final segmentation.

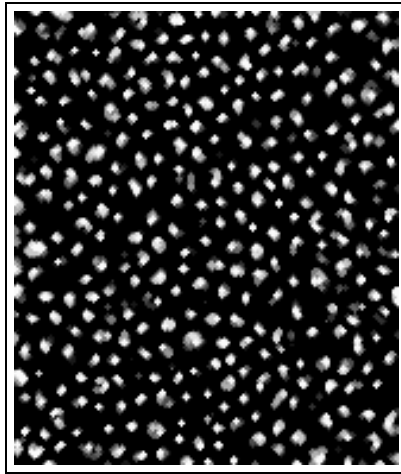
In addition to giving accurate results, this segmentation method relies on very few parameters, which ensures its robustness. Furthermore, all the operations involved are implemented in an optimized way, based on algorithms described in [23, 24, 27, 25]: The entire segmentation process takes only a few seconds on a workstation.

5 Data Analysis

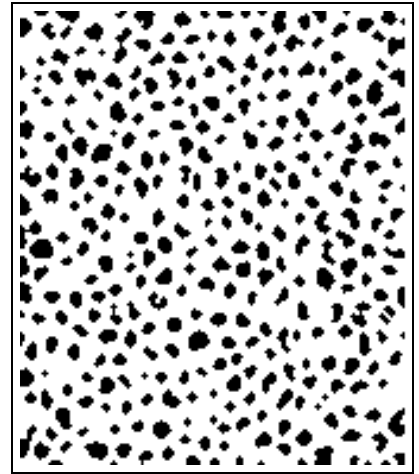
The segmentation described results in binary images of the corneal tissue in which two adjacent cells are separated by a line one pixel thick. In the present section we are concerned with extracting information from these images in order to characterize the healthiness of the cornea. Here, we could perfectly have used the binary images resulting



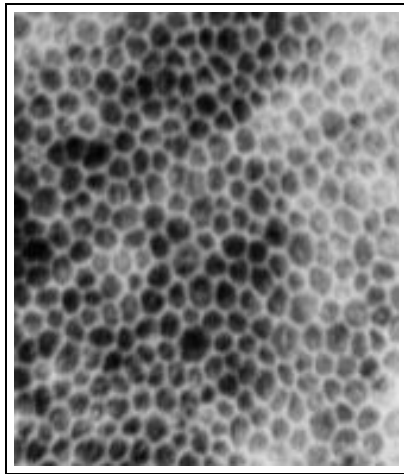
(a) after reconstruction



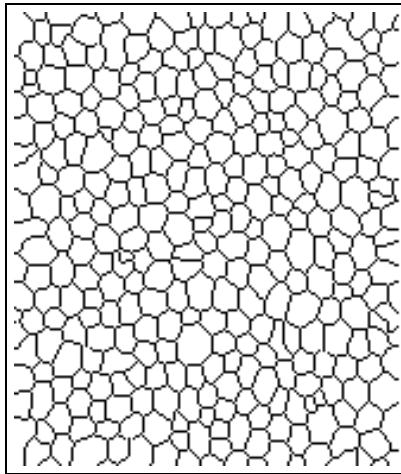
(b) extracted domes



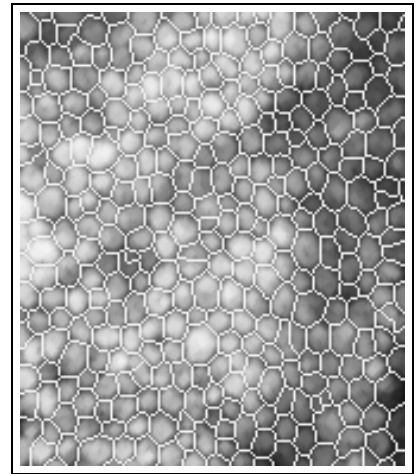
(c) cell markers



(d) inverted original image



(e) watershed segmentation



(f) result overlaid on original image

Figure 3: Illustration of the segmentation method

from our prior segmentation step. However, a consistent set of grayscale images of cornea at different ages was not available. Therefore, in the present section and the followings, we had to make use of older data, previously collected through the manual tracing of corneal endothelial tissue images. These images were digitized and a simple binary processing allowed us to obtain the binary images shown in Figs. 4(a)–(c), corresponding to corneas at increasing levels of deterioration.

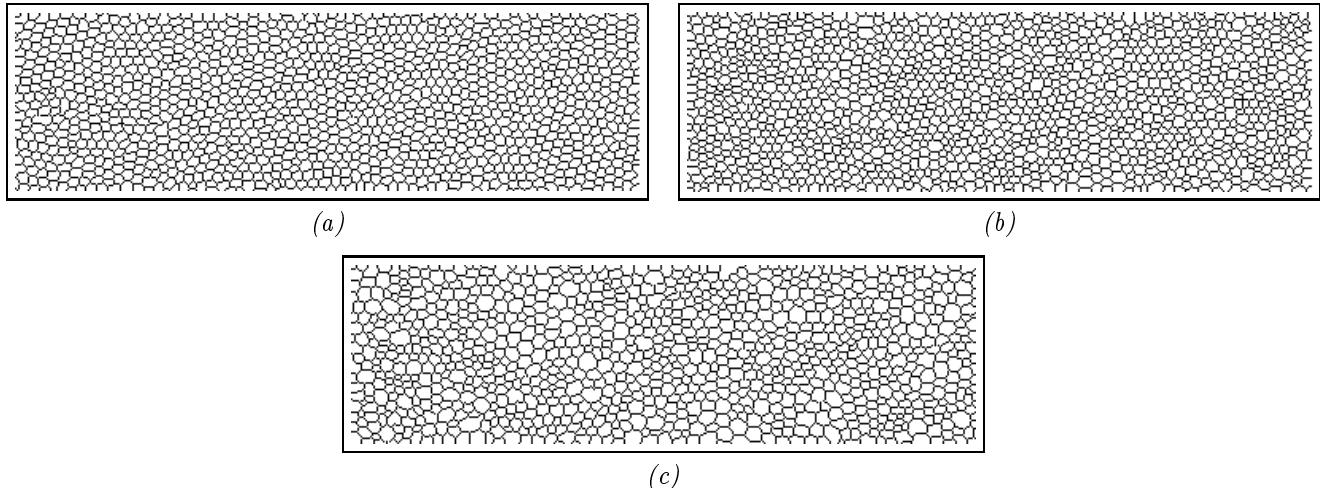


Figure 4 : Three different cases of segmented binary images

5.1 Size and shape of the cells

These images exhibit an increasing level of disorder. As mentioned in the introduction, this is due to the fact that with aging, corneal cells die and are not replaced by new cells via cell division, as in other bodily tissues. Here, the neighboring cells elongate to fill in the gap left by the dead cell. Therefore, with aging, many cells tend to become bigger. This phenomenon can be brought to light by simply assigning to each cell of Figs. 4(a)–(c) a gray-level value equals to its area (number of pixels). The resulting images are shown in Figs. 5(a)–(c). The gray-level information contained in these images makes the phenomenon of disorder appear even more clearly¹. Fig. 6 shows that the histograms of cell sizes for the three cases (a), (b) and (c) are increasingly distributed.

Classic morphological granulometries can also be used on Figs. 5(a)–(c). Recall that, given a convex structuring element B , whose homothetics are denoted $(B_n)_{n \geq 0}$:

$$\begin{aligned} B_0 &= \{\bar{\sigma}\} \\ B_1 &= B \\ \forall n \geq 1, B_{n+1} &= B_n \oplus B, \end{aligned}$$

the family of openings $(\gamma_{B_n})_{n \geq 0}$ constitutes a granulometry, as defined by Matheron [13]. The corresponding granulometry function $g(I)$ of a binary image I is then given by [26, 24]:

$$g(I) \begin{pmatrix} D_I & \longrightarrow & \mathbf{Z} \\ p & \longmapsto & \min\{k \in \mathbf{Z}^+ \mid \gamma_{B_k}(p) = 0\}. \end{pmatrix}$$

In other words, $g(I)$ associates with every pixel p of I the largest n such that $\gamma_{B_n}(I)(p) = 1$. The granulometry function of image 4(b) with respect to a family of squares is shown in Fig. 7. This image is quite similar to Fig. 5(b), which accounts for the fact that our corneal cells are convex polygons with little elongation. The same remark is valid for Figs. 4(a) and (c). Therefore, granulometric analysis of our images does not yield much useful additional quantitative information.

¹Note that the 5 lightest-colored cells of image 5(a) correspond to segmentation errors where two cells have been connected into one!

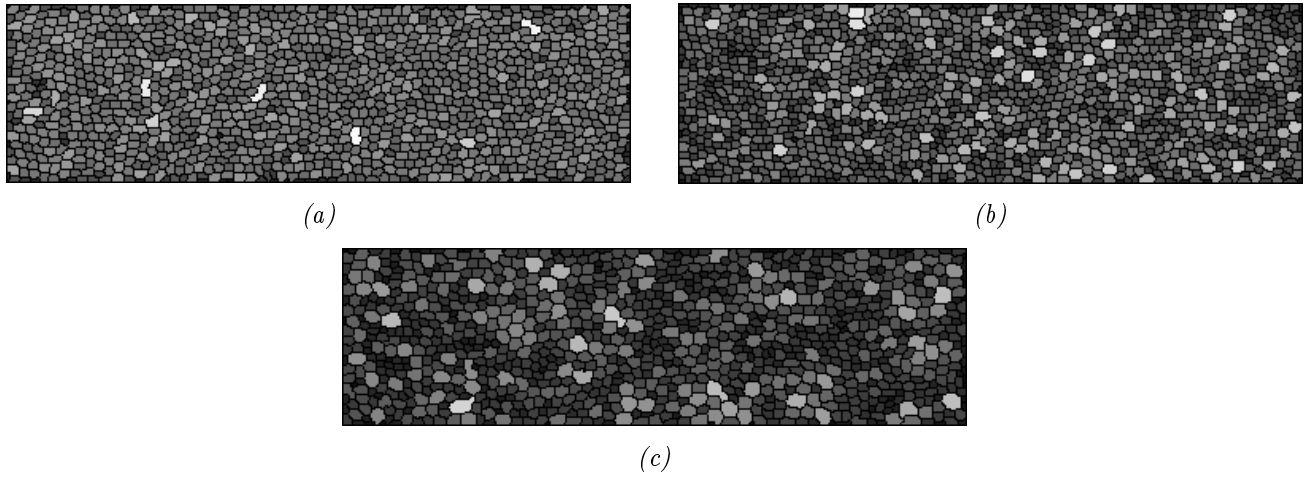


Figure 5 : After assigning to each cell of the tissues in Fig. 4 a value (gray-level) equal to its area.

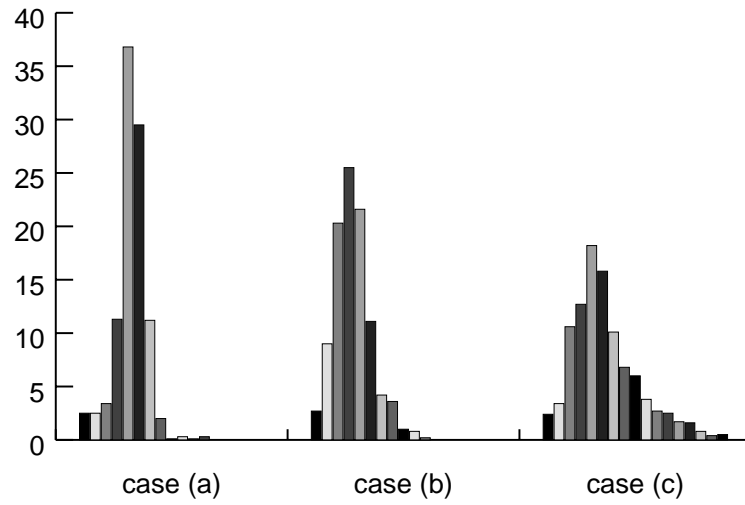


Figure 6 : Histograms of corneal cell sizes for Figs. 4(a)–(c).

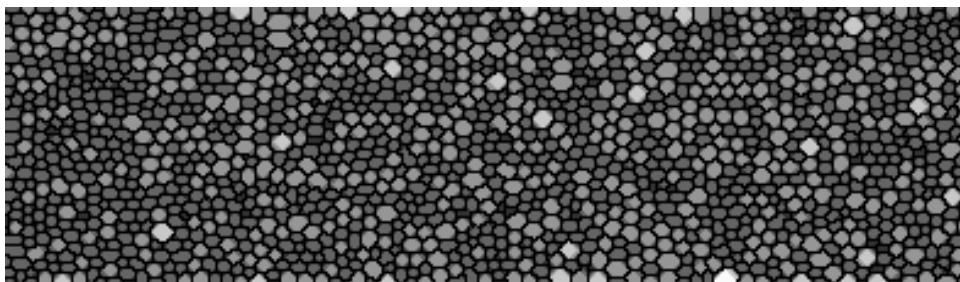


Figure 7 : Granulometry function of image 4(b).

The growth of the corneal cells is accompanied by a modification of their number of edges: as cells grow and alter their shapes to fill in the gap left by a dead cell, some of these polygonal cells increase their number of edges, while others end up with a smaller number of edges. An attempt at modeling this phenomenon is proposed in section 6. To determine the number of edges of a corneal cell, it suffices to extract its number of neighboring cells. To this purpose, we use contour tracking algorithms described in [22] to determine the adjacency graph of the corneal tissue: This graph is a triangulation in which every vertex corresponds to a unique cell. There is also a one to one correspondence between the edges of this triangulation and the neighborhood relationships between cells of the initial tissue (see Fig. 8). Using this graph, it is straightforward to assign to each cell its number of neighbors, as is done in Fig. 9².

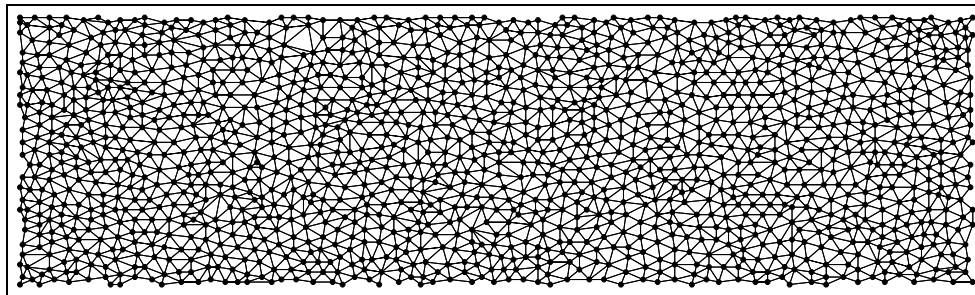


Figure 8 : Adjacency graph of the cells of image 4(b).

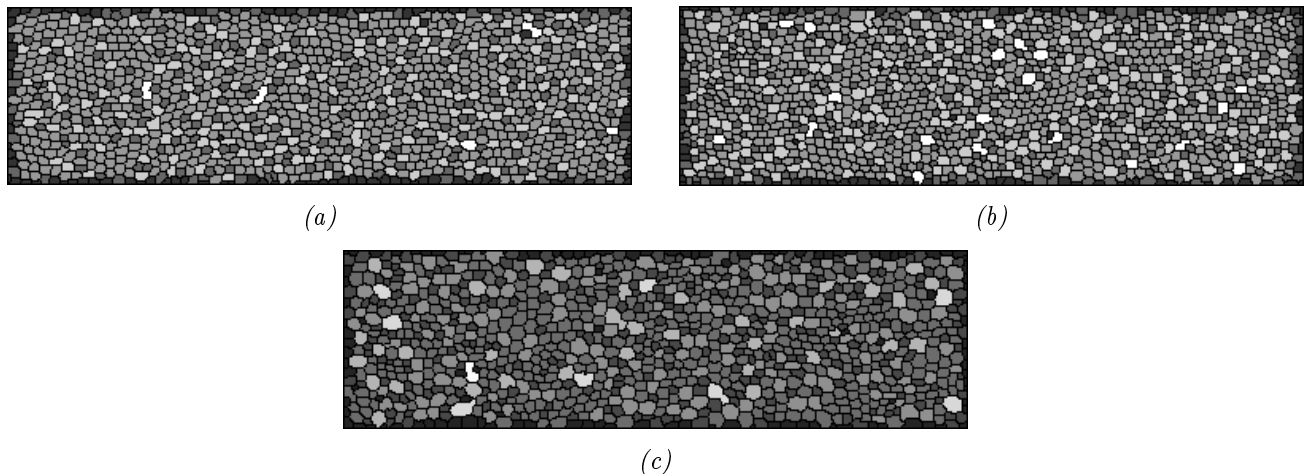


Figure 9 : Assigning to the cells of the images in Fig. 4 a gray-level equal to their number of neighbors.

This figure illustrates the same trend as Fig. 5, namely an increasing number of disorder, characterized by the increasing number of cells with 5, 7 or even 8 neighbors from (a) to (c). The histograms of cell number of neighbors for cases (a), (b) and (c) are shown in Fig. 10. Up to some scaling coefficients, these histograms are very similar to those of Fig. 6. This shows the strong—and intuitively clear—correlation existing between size and number of edges of the corneal cells. Due to their fewer number of possible values (the number of edges basically varies between 3 and 8), these histograms of number of neighbors are easier to interpret than the size histograms. Therefore, from now on, we shall focus on the number of neighbors of our corneal cells.

5.2 Spatial distribution of the corneal cells

Now that we have characterized the size and shape of our cells, we want to know whether the cell death phenomenon occurs with equal probability across the whole tissue. In other words, we would like to find out if cells tend to die at

²For the sake of display, the cells on the border of the image have been assigned value 4.

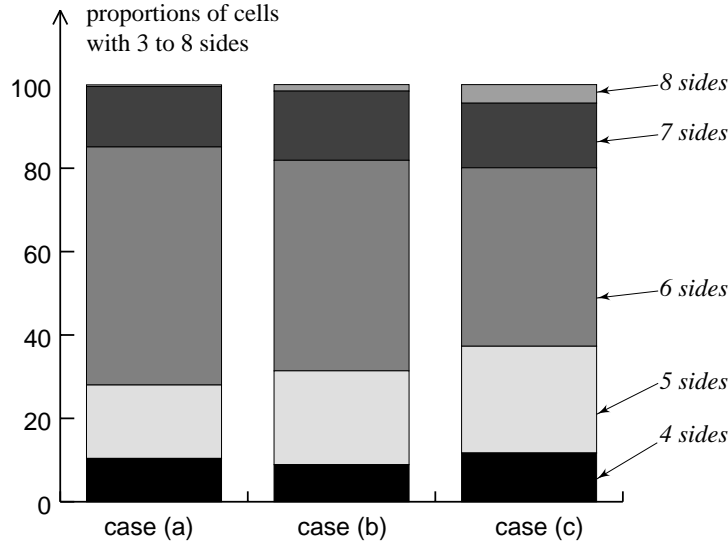


Figure 10 : Histograms of the number of neighbors for Figs. 4(a)–(c).

specific locations, like for example around large cells. Since the appearance of large and—to a lesser extend—small cells (resp. cells with many and few neighbors) is directly related to cell death, it seems interesting to study their distribution in the rest of the corneal tissue.

To this end, we applied morphological tools originally described in [21] and detailed in [22, 7], namely granulometries on graphs. Recall that, given a non-oriented graph $G = (V, E)$, with V as set of vertices and E as set of edges, and f a mapping from V to the set of real numbers \mathbb{R} , the elementary graph-dilation of f , denoted $\delta(f)$, is characterized by:

$$\forall v \in V, \delta(f)(v) = \max\{f(v') \mid v' = v \text{ or } (v, v') \in E\}.$$

In simpler terms, graph-dilating f is equivalent to assigning to each vertex v the maximal value of f on the vertices in the neighborhood of v . Erosions, openings and closings on graphs can be defined in the same way [21].

In the present study, the graph structure is given by the triangulation (see Fig. 8) and the mapping f associates with each vertex the number of neighbors of the corresponding cell. Performing a granulometry by closings of this graph allows us to bring to light the clusters of cells with large number of neighbors, as illustrated by Fig. 11. For each closing of size $k > 0$, we compute the granulometry coefficient $C_f(k)$ as:

$$C_f(k) = \frac{\sum_{v \in V} \phi_k(f)(v) - \sum_{v \in V} \phi_{k-1}(f)(v)}{\sum_{v \in V} f(v)},$$

where $\phi_k(f)$ denotes the graph-closing of size k of f .

The granulometric curves thus extracted for the graphs constructed from Figs. 4(a)–(c) are shown in Fig. 12. These three curves are relatively similar, which is a good argument in favor of an even distribution of the cell death sites across the corneal tissue. Note that in order not to introduce any bias in our granulometric analysis, the vertices corresponding to cells on the border of the image were initially given value 0. Similar analyses can be performed by openings, and also on the “binary graph” constructed by giving value 1 to the cells with 6 neighbors and value 0 to the others.

6 Model of corneal cell tissue aging

Our better understanding of the corneal endothelial cell tissue will now serve to:

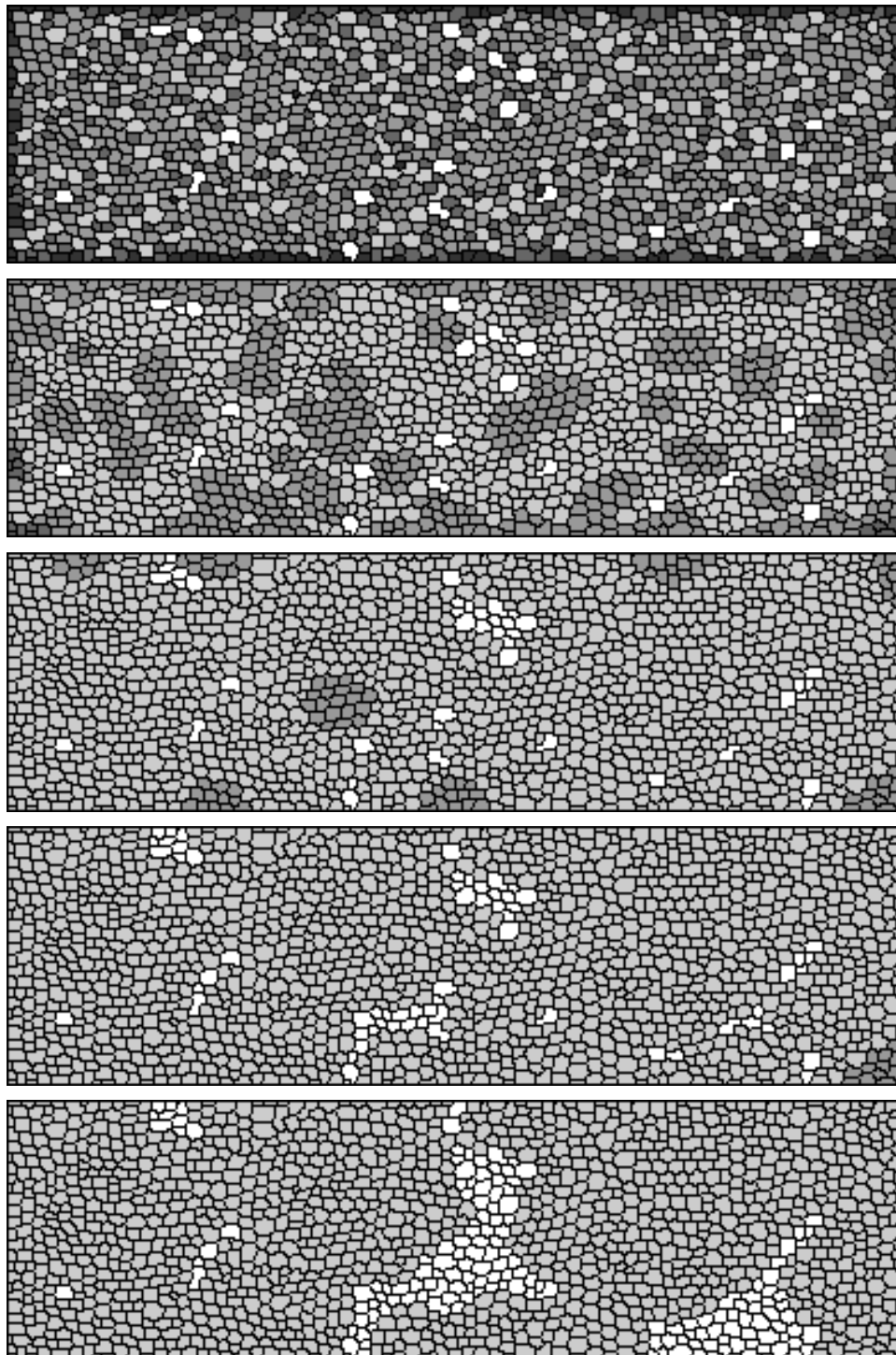


Figure 11 : Granulometry of the graph displayed in image 9(b) using closings of increasing size.

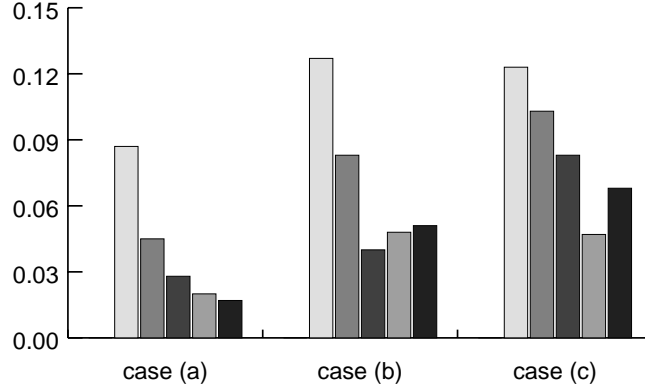


Figure 12 : Graph-granulometric curves corresponding to Figs. 4(a)–(c).

1. propose a model for corneal cell death and rearrangement of corneal tissue
2. verify the accuracy of this model by matching its output with the numerical results obtained in section 5.

Granulometric analyses proved that no clusters of large cells or small cells can be observed in our data. We concluded that the distribution of the cell death sites was relatively uniform in the corneal tissue. This leads to our first assumption:

|| *At any given time, the cell death probability is evenly distributed.*

Let us now consider the case where a cell c with n edges dies. As the surrounding cells elongate to fill in the gap left by this death, experimentally confirmed physics rules state that the resulting tissue configuration will be stable. In other words, the resulting cells still constitute a regular tessellation, where no boundary point can be shared by more than three cells. At the same time, as can be clearly seen on Figs. 1 and 4(a)–(c), these cells remain polygonal and convex.

Suppose for example that the number of edges of c is $n = 5$. Let us denote the neighbors of c by c_1, c_2, \dots, c_5 . In order to find out the possible cell configurations resulting from the death of c , we first extend the edges between the c_i and c_{i+1} , $i = 1$ to 4 , and between c_5 and c_1 in such a way that they meet at a point p . Note that too do so, we often have to slightly modify the orientation of these edges. In this process, all the c_i lose an edge (see Fig. 13). We then move slightly backwards one of these intersection points so that it does not lie on p any more. This has the effect of giving back an edge to two of the c_i 's. By repeating this process another time, we end up with a regular tessellation, as illustrated by the lower left corner of Fig. 13.

The same technique can be used to exhaustively enumerate all the possible cell configurations resulting from the death of a cell with an arbitrary number of edges, with their associated probabilities. In the case of a cell with 5 edges we find that:

- 2 of the neighboring cells lose an edge
- the number of edges of 2 cells remains unchanged
- one cell gains an edge

(see Fig. 13). We say that the pattern attached to the death of a 5-sided cell is $(-1, -1, 0, 0, +1)$.

Similar studies can be made for cells with different number of neighbors. To summarize, we found the following patterns:

- death of a 3-sided cell: $(-1, -1, -1)$
- death of a 4-sided cell: $(-1, -1, 0, 0)$
- death of a 5-sided cell: $(-1, -1, 0, 0, +1)$
- death of a 6-sided cell: $(-1, -1, 0, 0, +1, +1)$ with probability $2/5$, $(+1, +1, +1, -1, -1, -1)$ with probability $1/5$ and $(-1, -1, 0, 0, 0, +2)$ with probability $2/5$.

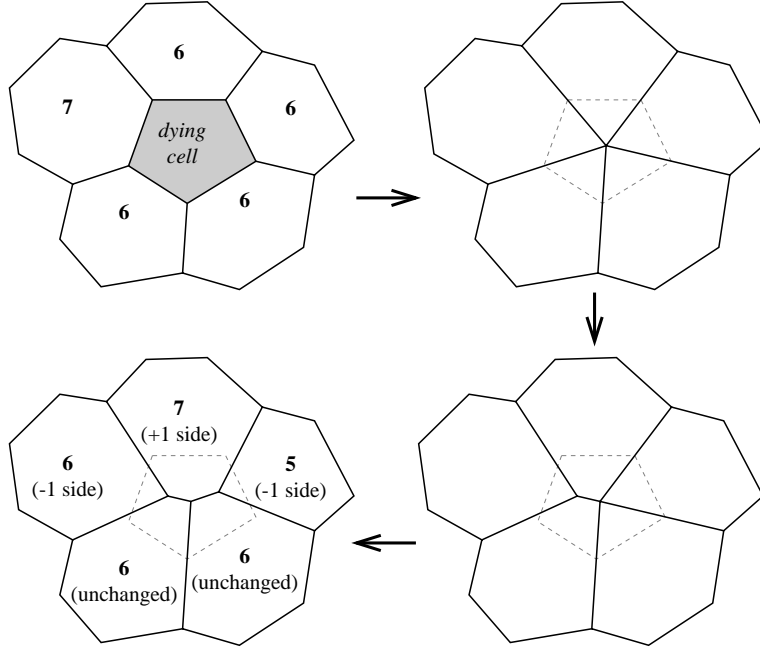


Figure 13: Model of the rearrangement following the death of a 5-sided cell.
The numbers inside the cells represent their number of sides.

We made the simplifying assumption that cells with more than 7 edges cannot die directly. Additionally, the results of section 5 made it reasonable to assume that the number of neighbors of a given cell would never exceed 8. Finally we also assumed that a 3-sided cell can never lose an edge during a cell rearrangement.

Let us denote by $c(t)$ the cell concentration at time t and $c_3(t), c_4(t), \dots, c_8(t)$ the concentrations of the 3-sided, 4-sided, \dots , 8-sided cells respectively. Obviously,

$$c(t) = \sum_{i=3}^{i=8} c_i(t)$$

Let also $c'(t) = c_3(t) + c_4(t) + c_5(t) + c_6(t)$. Assume that between time t and time $t + 1$, a cell dies. The probability for it to be a k -sided cell is $p_k(t) = c_k(t)/c'(t)$. If this cell is, for example, a cell with 5 sides, one can show that the resulting cell concentrations $c_i(t + 1)$ at time $t + 1$ are:

$$\begin{aligned} c_3(t + 1) &= c_3(t) + 2 \frac{c_4(t)}{c(t) - c_3(t)} \\ c_4(t + 1) &= c_4(t) - 2 \frac{c_4(t)}{c(t) - c_3(t)} - \frac{c_4(t)}{c(t) - c_8(t)} + 2 \frac{c_5(t)}{c(t) - c_3(t)} \\ c_5(t + 1) &= c_5(t) - 1 - 2 \frac{c_5(t)}{c(t) - c_3(t)} - \frac{c_5(t)}{c(t) - c_8(t)} + 2 \frac{c_6(t)}{c(t) - c_3(t)} + \frac{c_4(t)}{c(t) - c_8(t)} \\ c_6(t + 1) &= c_6(t) - 2 \frac{c_6(t)}{c(t) - c_3(t)} - \frac{c_6(t)}{c(t) - c_8(t)} + 2 \frac{c_7(t)}{c(t) - c_3(t)} + \frac{c_5(t)}{c(t) - c_8(t)} \\ c_7(t + 1) &= c_7(t) - 2 \frac{c_7(t)}{c(t) - c_3(t)} - \frac{c_7(t)}{c(t) - c_8(t)} + 2 \frac{c_8(t)}{c(t) - c_3(t)} + \frac{c_6(t)}{c(t) - c_8(t)} \\ c_8(t + 1) &= c_8(t) - 2 \frac{c_8(t)}{c(t) - c_3(t)} + \frac{c_7(t)}{c(t) - c_8(t)} \end{aligned}$$

By combining the equations corresponding to the death of a cell with k sides, $k = 3$ to 6, with their respective probabilities, we come up with a model describing the evolution of the cell concentrations c_i , $i = 3$ to 8 as a function

of the proportion of cells having died in the tissue. Its equations would be a bit too long to fit in this paper! Numerical simulations were performed, using the following initial conditions:

$$c_3(0) = c_4(0) = c_5(0) = c_7(0) = c_8(0) = 0 \quad \text{and} \quad c_6(0) = 1.$$

The corresponding histograms of cell concentrations are displayed in Fig. 14.

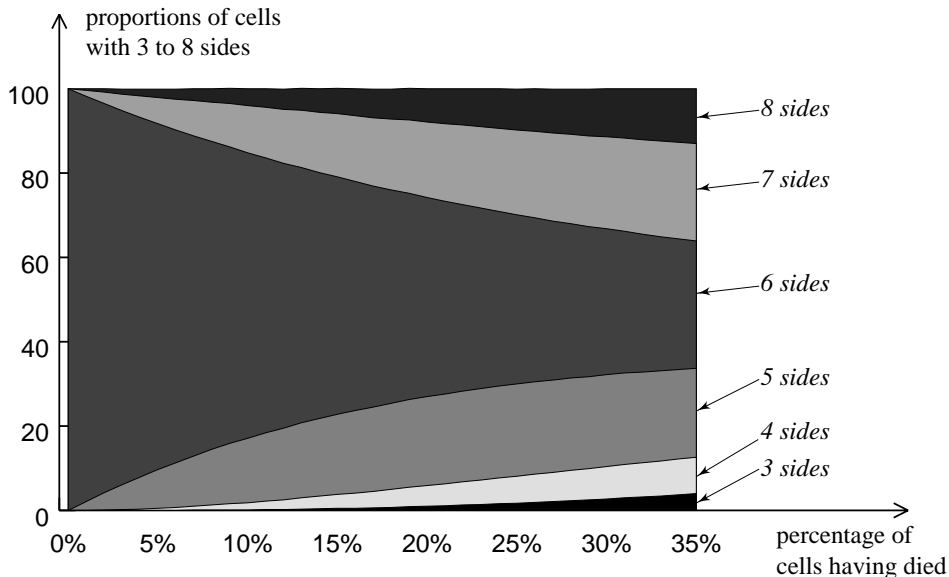


Figure 14 : Histograms of cell concentrations provided by our model.

The simplifying assumptions we made, namely:

- cells with more than 7 sides cannot die
- cells can never have more than 8 edges
- at any given time, all the cells have the same probability of dying
- the tissue has no boundary (no edge effects taken into account)

explain the growing mismatch that can be observed as the proportion of dead cells increases. The most noticeable effect (directly related to assumption 1) is that too much weight is given to the 8-sided cells, and to a lesser extent, to the 7-sided ones.

However, even with this very crude model, comparing the histograms experimentally found (see Fig. 10) with this simulation shows a very good match for the concentrations of cells with 5, 6 and 7 sides. This allows us to propose estimates for the proportion of cells having died in the corneal tissues of Fig. 4:

- ||| **case (a)** 15%
- ||| **case (b)** 18%
- ||| **case (c)** 23%.

7 Conclusions

In this paper, we proposed a new method for segmenting grayscale images of corneal endothelial tissue. Contrary to the algorithms proposed in literature, this method does not rely on adaptive thresholding or top-hat transformations,

but on a morphological dome extractor coupled with the watershed transformation. Experiments showed the greater accuracy and robustness of this approach.

The binary images of corneal tissue resulting from this segmentation step were then analyzed and size distributions of the cells were calculated. Neighborhood graphs of the cells were determined and allowed us to easily extract the distribution of the number of neighbors (i.e. number of edges) of the cells. Granulometric analyses of the graphs themselves also showed that the cells with larger number of edges (resp. small number of edges) are relatively evenly distributed in the tissue: this proves that the cell death phenomenon does not occur only at specific locations but with even probability across the whole tissue.

Lastly, we were able to propose a model for the corneal cell death phenomenon. Computational complexity considerations led us to make several simplifying assumptions which are probably unrealistic. For example, the assumption that the cells with more than 7 edges cannot die results in a too large number of cells with 7 or 8 edges. However, especially when restricted to relatively “young” corneas (where less than 25% cells have died), numerical simulations of this model matched experimental results quite well. We were therefore able not only to simulate the dynamics of corneal cell death, but also to propose an estimate for the percentage of cells having died in our test cornea images. A refined version of this model is under development. Together with the segmentation technique proposed in section 4, this could lead to an incredibly useful diagnostics tool for corneal pathologies.

8 References

1. Y.-K. L. B. Masters and W. Rhodes. Fourier transform method for statistical evaluation of corneal endothelial morphology. In B. Masters, editor, *Noninvasive Diagnostic Techniques in Ophthalmology*, pages 122–141. Springer Verlag, New York, 1990.
2. S. Beucher and C. Lantuéjoul. Use of watersheds in contour detection. In *International Workshop on Image Processing, Real-Time Edge and Motion Detection/Estimation*, Rennes, France, 1979.
3. G. Cazuguel and F. Mimouni. Extraction automatique des contours cellulaires de l’endothelium cornéen humain. *Innov. Tech. Biol. Med.*, 10(6):659–667, 1989.
4. E. Fabian, M. Mertz, and W. Koditz. Endothelmorphometrie durch automatisierte fernsehbildanalyse. *Klin Monatsbt. Augenheilkd.*, 182:218–223, 1983.
5. C.-S. Fuh, P. Maragos, and L. Vincent. Region-based approaches to visual motion correspondence. Technical report, HRL, Harvard University, Cambridge, 1991. Submitted to PAMI.
6. M. Grimaud. A new measure of contrast: Dynamics. In *SPIE Vol. 1769, Image Algebra and Morphological Image Processing III*, pages 292–305, San Diego CA, July 1992.
7. H. Heijmans and L. Vincent. Graph morphology in image analysis. In E. R. Dougherty, editor, *Mathematical Morphology in Image Processing*, pages 171–203. Marcel-Dekker, Sept. 1992.
8. D. Jeulin, L. Vincent, and G. Serpe. Propagation algorithms on graphs for physical applications. *JVCIR*, 3(2):161–181, June 1992.
9. C.-J. Koester, C.-W. Roberts, A. Donn, and F.-B. Hoeffle. Wide field specular microscopy. *Ophthalmology*, 87:849–860, 1980.
10. R.-A. Laing, J.-F. Brenner, J.-M. Lester, and J.-L. Mcfarland. Automated morphometric analysis of endothelial cells. *Invest. Ophthalmol. Vis. Sci.*, 20:407–410, 1981.
11. C. Lantuéjoul. Issues of digital image processing. In R. M. Haralick and J.-C. Simon, editors, *Skeletonization in Quantitative Metallography*. Sijthoff and Noordhoff, Groningen, The Netherlands, 1980.
12. C. Lantuéjoul and F. Maisonneuve. Geodesic methods in quantitative image analysis. *Pattern Recognition*, 17(2):177–187, 1984.
13. G. Matheron. *Éléments pour une Théorie des Milieux Poreux*. Masson, Paris, 1967.
14. D. Mayer. *Clinical Wide Field Specular Microscopy*. Boilliere Tindall, London, 1984.

15. F. Meyer. Contrast feature extraction. In J.-L. Chermant, editor, *Quantitative Analysis of Microstructures in Material Sciences, Biology and Medicine*, Stuttgart, FRG, 1978. Riederer Verlag. Special issue of Practical Metallography.
16. F. Meyer and S. Beucher. Morphological segmentation. *Journal of Visual Communication and Image Representation*, 1:21–46, Sept. 1990.
17. C. Roberts and C. Koester. Video with wide-field specular microscopy. *Ophthalmology*, 88, 1981.
18. J. Serra. *Image Analysis and Mathematical Morphology*. Academic Press, London, 1982.
19. J. Serra, editor. *Image Analysis and Mathematical Morphology, Volume 2: Theoretical Advances*. Academic Press, London, 1988.
20. J. Serra and L. Vincent. An overview of morphological filtering. *Circuits, Systems and Signal Processing*, 11(1):47–108, Jan. 1992.
21. L. Vincent. Graphs and mathematical morphology. *Signal Processing*, 16:365–388, Apr. 1989.
22. L. Vincent. *Algorithmes Morphologiques à Base de Files d'Attente et de Lacets: Extension aux Graphes*. PhD thesis, Ecole des Mines, Paris, May 1990.
23. L. Vincent. New trends in morphological algorithms. In *SPIE/SPSE Vol. 1451, Nonlinear Image Processing II*, pages 158–169, San Jose, CA, Feb. 1991.
24. L. Vincent. Morphological algorithms. In E. R. Dougherty, editor, *Mathematical Morphology in Image Processing*, pages 255–288. Marcel-Dekker, Inc., New York, Sept. 1992.
25. L. Vincent. Morphological grayscale reconstruction: Definition, efficient algorithms and applications in image analysis. In *IEEE Int. Computer Vision and Pattern Recog. Conference*, pages 633–635, Champaign IL, June 1992.
26. L. Vincent and S. Beucher. The morphological approach to segmentation: an introduction. Technical report, Ecole des Mines, CMM, Paris, 1989.
27. L. Vincent and P. Soille. Watersheds in digital spaces: an efficient algorithm based on immersion simulations. *IEEE Trans. Pattern Anal. Machine Intell.*, 13(6):583–598, June 1991.
28. J.-H. Yu, M.-M. Hsieh, J.-L. Su, and B.-N. Hung. Algorithm for Automatic Analysis of Corneal Endothelial Images. In *13th Annual International Conf. of the IEEE Engineering in Medicine and Biology Society*, pages 273–275, 1991.